Long-Range VNA-Based Channel Sounder: Design and Measurement Validation at mmWave and sub-THz frequency bands

Bengtson, Mikkel Filt; Lyu, Yejian; Fan, Wei

Published in:
China Communications

Publication date:
2022

Document Version
Accepted author manuscript, peer reviewed version

Long-Range VNA-Based Channel Sounder: Design and Measurement Validation at mmWave and sub-THz frequency bands

Mikkel Bengtson, Yejian Lyu, Wei Fan

***Abstract*—With the increasing demand for high bandwidth wireless communication systems, and with a congested spectrum in the sub-6 GHz frequency bands, researchers have been looking into exploration of millimeter wave (mmWave) and sub-terahertz (sub-THz) frequency bands. Channel modeling is essential for system design and performance evaluation of new wireless communication systems. Accurate channel modeling relies on reliable measured channel data, which is collected by high-fidelity channel sounders. Furthermore, it is of importance to understand to which extent channel parameters are frequency dependent in typical deployment scenario (including both indoor short-range and outdoor long-range scenarios). To achieve this purpose, this paper presents a state-of-art long-range 28 GHz and 300 GHz VNA-based channel sounder using optical cable solutions, which can support a measurement range up to 300 m and 600 m in principle, respectively. The design, development and validation of the long-range channel sounders at mmWave and sub-THz bands are reported, with a focus on their system principle, link budget, and back-to-back measurements. Furthermore, a measurement campaign in an indoor corridor is performed using the developed 300 GHz system and 28 GHz channel sounding systems. Both measured channels at the 28 GHz and 300 GHz channels are shown to be highly sparse and specular. A higher number of Multi Path Components (MPC) are observed for the 28 GHz system, while the same main MPC are observed for both systems.**

***Index Terms*—mmWave, Channel Sounding, sub-THz, radio propagation, beyond 5G communications**

I. Introduction

With the 5G networks starting to commercially roll out, academia and industries have started to look into the beyond-5G and 6G communication systems [1]. Communication system application such as autonomous driving, Internet of Things (IOT), health care (remote operation) and high data rate backhaul links, will require data rates which current systems and bandwidths are unable to achieve [2]. The growing demands for higher data rates have motivated the research towards higher frequency ranges covering from 100 GHz to 10 THz which is currently largely unused. Specifically, frequency bands at 100 GHz - 300 GHz, named sub-Terahertz (sub-THz) in this paper, are currently a hot research topic. Furthermore, standardization organizations and countries have started standardizing and allocating frequency bands in the sub-THz region. The IEEE 802.15.3d published in 2017 defined a new physical layer standard for sub-THz wireless networks at 250 Ghz to 325 Ghz [3]. In 2019, the Federal Communication Commision (FCC) started to expand the spectrum licenses for spectrum over 95 GHz for experimental purposes [4]. Note that frequency allocations for 6G communication systems are still in its premature stage, though there are active discussions ongoing.

Investigation in atmospheric absorption of electromagnetic waves at sub-THz frequencies shown that certain frequency bands at sub-THz have high attenuation, limiting the useability for long-range cellular communications [5]. Specifically, the frequency bands at 120 GHz and 183 GHz have shown high attenuation compared to other frequency bands. While the frequency bands at 140 GHz and 240 GHz have shown less attenuation, making it more suitable for long-range communications [6]. The path losses are considerable at sub-THz bands, and therefore, high-gain directive antennas need to be employed [5], [7].

Channel characteristics and models are of importance when developing and deploying communication systems. Both large-scale parameters such as pathloss (PL) and shadowing, and small-scale properties, e.g. delay spread and angle spread are important characteristics of wireless channels [8]. There has been growing interest on sub-THz channel modeling research. For example, channel models for frequencies up to 100 GHz are reported in [9]. Since the wavelength at sub-THz bands approaches the size of dust and rain it might alter the wireless propagation channel properties compared to lower frequencies, it is therefore essential to understand the frequency dependence of channel parameters [2]. Measurement campaigns with channel sounder system for measuring at 140 GHz and 300 GHz are currently being developed and massive channel measurements are being carried out [10]–[15].

Different measurements at 140 GHz have been carried out [6], [16]–[19]. In [6], penetration loss of different materials were explored and it was found that the losses were higher compared to those in lower frequencies. In [16] short range Line of Sight (LOS) and Non Line of Sight (NLOS) measurements were performed with a human blocking the LOS path. Measurements in an office environment were performed in [17], where a sparse number of secondary NLOS MPCs were found. Outdoor urban environment measurements at 140 GHz were performed in [18], where the Power Angular spectrum (PAS) was explored. In [20] long-range measurements in a shopping mall and airport with distances of up to 60 m were performed, large-scale parameters, e.g. path loss were

Mikkel Bengtson, Yejian Lyu, Wei Fan are with the Antenna Propagation and Millimeter-wave Systems (APMS) section, Aalborg University, Denmark. (Corresponding author: Wei Fan; Email: wfa@es.aau.dk)

investigated. In [19] a comparison between mmWave and sub-THz frequency bands, i.e. 28 GHz and 140 GHz, was made at a shopping mall environment where Receiver (Rx) and Transmitter (Tx) were placed with distances up to 60 m. It was observed that a higher amount of delay and angular spread were observed at 28 GHz compared to 140 GHz. Similar results were found between frequencies of 100 GHz and 300 GHz with a short measurement distance [11].

The deployment scenarios for 5G and future communication systems are envisioned to be similar as the 4G communication scenarios, e.g. indoor hotspot and urban micro- (UMi) and urban macro- (UMa) cellular scenarios [21]. However, few literature have reported the channel measurements and modeling in the long-range scenarios, e.g. airport and outdoor urban street, which are one of the main communication scenarios for 5G and future communication. Several channel soundings at mmWave bands in the long-range deployment scenario have been reported in [21]–[27]. Channel measurements were performed in the typical long-range indoor scenarios, e.g. large hall [22], shopping mall [23], and airport [24] and in outdoor scenarios in [21], [25]–[27].

Measurements for 300 GHz have been performed in different scenarios. Short range indoor channel measurements have been performed in [11], [28]–[31]. Reflections and edge diffraction were investigated in [28], and a LOS measurement was performed in a small room with a Tx-Rx distance of 1 m. Measurements in a laboratory room with a distance of 2.25 m were performed [11]. Outdoor train to train measurements at 300 GHz were performed in [32], where the measurements with a Tx-Rx distance of 6.7 m placed close to trains were made. Channel measurements in an environment with standing cars were explored in [33], where different measurement scenarios such as LOS with under-vehicle and side-reflection from cars in another lane were performed.

High-fiderlity channel sounders are essential to collect reliable measured channel data. The pulse-based channel sounder, i.e. THz Time-domain Spectrometer (THz-TDS), has primarily been used for material characterization due to the limited dynamic range [34], [35]. A 140 GHz correlation-based sounder is presented by [6] achieving a dynamic range of 145 dB. A correlation-based channel sounding system working at 300 GHz is presented in [36] achieving dynamic ranges of 60 dB and limited in range between the Tx and Rx to 20 m. To achieve measurement capability at sub-THz frequencies for the vector network analyzer (VNA), frequency extension modules are used [11]. High RF cable losses at high frequencies would limit the achievable dynamic range and thereby the measurement range [37]. With the use of Radio over Fiber (RoF) the cable losses can be mitigated [18], [22]. VNA based channel sounder systems have been developed for 140 GHz achieving a dynamic range of up to 130-140 dB [18], [19]. For 300 GHz VNA based channel sounder system dynamic ranges for up to 90 dB have been achieved [38]. Furthermore, frequency dependence has been explored with comparisons between 140 GHz and 28 GHz [19].

The scope of this paper is to present a state-of-the-art Vector Network Analyzer (VNA) based long-range channel sounding scheme design and validation for sub-THz bands. The channel sounder system design, functionality and link budget will be presented along with a long-range measurement in a corridor scenario. We also aim to determine how the channel parameters are changed over the frequency band. To understand the frequency dependence of channel parameters in the mmWave and sub-THz frequency region, a long-range VNA channel sounder at mmWave bands is developed and validated as well. The comparison measurement at the 28-30 GHz and 299-301 GHz is performed. The authors have found that few works have been reported in the literature to compare measured channels at 28 GHz and sub-THz bands for long-range scenarios.

The rest of the paper is organized as follows: The long-range 28 GHz channel sounder system and 300 GHz channel sounder system with link budget are presented in Section II . Section III describes the measurement setup for the comparative measurement. The measurement results are presented in Section IV. Lastly, conclusion of this work and the future work are made in Section V.

II. Channel Sounder System

Long-range channel sounding systems at 28 GHz and 300 GHz are described in this section. Both of the channel sounding systems will be presented, with a detailed link budget analysis. First in Section II-A, the 28 GHz system is described followed by a description of the 300 GHz system in Section II-B. Both systems use RoF techniques to mitigate the cable losses.

A. 28 GHz Channel Sounding System

In Fig. 1, a block diagram of the designed 28 GHz system is shown. The specific components used can be seen in Table I. The output of port 1 from the VNA is connected to a laser, which converts the electric signal to an optical signal. Compared to the high signal loss in the RF coaxial cables (e.g. 1.59 dB/m at 30 GHz), an increase in distance can be achieved, since the signal loss in the optical fiber cable is lower (e.g. 0.4 dB/km) [22]. The optical signal is afterward converted to an electrical signal by a photo detector. The signal is amplified before transmission to increase the dynamic range of the system. At the Rx side the antenna is directly connected to the VNA by a coaxial cable. That is, only remoting of the Tx antenna is employed in the designed system. From Fig. 1, the back-to-back calibration point is also shown. An optical fiber cable of 300 m is employed in the designed system. Note that the measurement system supports a measurement range up to 300 m in principle. However, the measurement range might be limited by the measurement scenario in practice. Also, we have to consider over-the-air free space propagation loss and misalignment loss (e.g. antenna rotation and polarization alignment) at the Tx and Rx antennas in practical measurements.

A link budget for the system is made and shown in Fig. 2. The output power of the VNA is set to -12 dBm. As seen the coaxial cables in the system attenuates the power around 8.7 dB in total even though the cable length is kept at a minimal. The optical link is composed of a laser, photo detector and

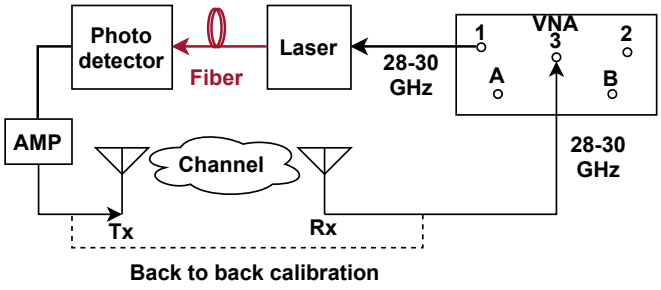

Fig. 1. Block diagram of the 28 GHz system

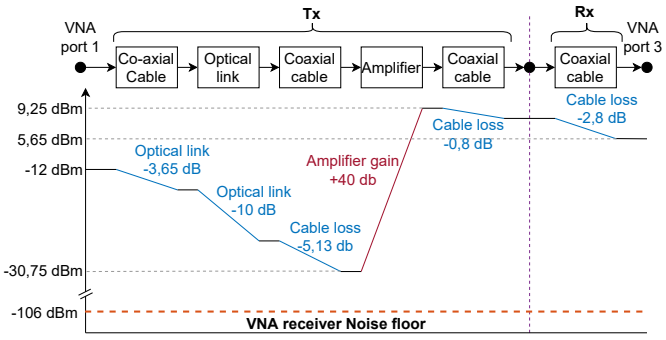

Fig. 2. Illustration of the link budget for the 28 GHz system. The link budget measurements are performed at 28 GHz.

fiber cables, which gives a total loss of -10 dB. Because of the high gain amplifier, a dynamic range of 100 dB can be obtained at an Intermediate Frequency (IF) Bandwidth (BW) of 1 kHz. Note that a lower IF bandwidth setting can improve the system dynamic range, which however would also increase the measurement time. Considering isotropic antennas with no directivity, the maximal achievable distance from the dynamic range is 79 m, according to the Friis transmission formula. Note that in typical mmWave channel sounding and communication systems, high-gain directional antennas are used to improve the measurement range.

B. 300 GHz Channel Sounding System

A block diagram of the 300 GHz system can be seen in Fig. 3, and the different components can be seen in Table I. Two different sets of laser/photo detectors are used. The laser/photo detector denoted high frequency (HF) is for the GHz signal i.e. 10-15 GHz for the 300 GHz system, and 28-30 GHz for the 28 GHz system. The laser/photo detector denoted low frequency (LF) are for the MHz reference signal. The system consists of the optical link, frequency extender and coaxial cable. The frequency extender system consists of a Tx extender and an Rx extender. The Tx extender is a 4 port device. The Radio Frequency (RF) port input signal has a frequency from around 12.22 to around 18.33 GHz (as explained below), and the signal is multiplied with an 18 times multiplier to a signal with frequency from 220 GHz to 330 GHz [39]. In the directional coupler, the signal is guided to the Test port which is directly connected to an antenna. The

TABLE I
SYSTEM COMPONENTS FOR 300GHZ CHANNEL SOUNDER

Part	300 GHz system	30 GHz system
VNA	Keysight PNA N5227B	
HF Laser	QMOD XMTQ-C-A-24	
HF Photo detector	QMOD XMRQ-C-A-24	
LF Laser	RF optics RFOF6T3FRPA11 Tx	-
LF Photo detector	RF optics RFOF6T3FRPA11 Rx	-
Optical splitter	JDS FFC-CKH12B105-003	-
Frequency Extender	VDI WR 3.4	-

reference signal is obtained by mixing the other output signal of the directional coupler and a Local Oscillator (LO) signal from the VNA. The reference signal is at a constant frequency of 7.44 MHz, and it is transmitted using an optical link to the VNA. The reference signal is obtained at the output of the mixer in the frequency extender and is shown in Equation (1).

$$f_{ref} = f_{Test\ port} - 24 f_{LO} \tag{1}$$

Where f_{ref},$f_{Testport}$ and f_{LO} is the reference frequency, the frequency at the test port and the LO frequency from port 3 at the VNA, respectively. The operational frequency range for the Test port of the frequency extender is from 220 GHz - 330 GHz, therefore the output of the VNA port 1 is from 12.22 GHz to 18.33 GHz and is shown rounded in Fig. 3. To obtain a fixed reference signal of 7.44 MHz, the output frequencies at port 3 of the VNA is calculated with Equation (2).

$$f_{LO} = \frac{18 f_{RF} - f_{ref}}{24} \tag{2}$$

Where f_{RF} is the frequency at the VNA port 1. The frequency for the LO is calculated to be from 9.17 GHz to 13.75 GHz and is also shown rounded in Fig. 3.

The LO signal to the frequency extender is transmitted through an optical link, to have the same reference frequency for both the Tx and Rx module. An optical splitter is used in the LO link. By using the same LO in the Tx module the reference signals frequencies are identical. The Rx extender receives the signal from the antenna directly at the Test port which is then mixed with the LO signal to obtain the reference signal.

Four optical fiber cables of length 300 m are employed for the system, leading to a maximum measurement distance of 600 m in principle. The link budget for the 300 GHz system is divided into 3 parts, the RF input for the Tx-extender, the LO chain and the reference port A to the reference port B. The frequency extender specifies certain power levels at the RF port and LO port. The system must be capable of delivering those power levels, and they do not contribute to the dynamic range of the system [39]. The link budget for the signal chain between the VNA port 1 and the RF port consist only of a coaxial cable. The output power from the VNA at port 1 is 9 dBm and the loss in the cable is -9 dB giving a power of 0 dBm at the RF port. Link budget for the LO chain can be seen in Fig. 4. The output power for the LO chain is set to 5 dBm, a loss of -10.5 dB from the optical link is measured,

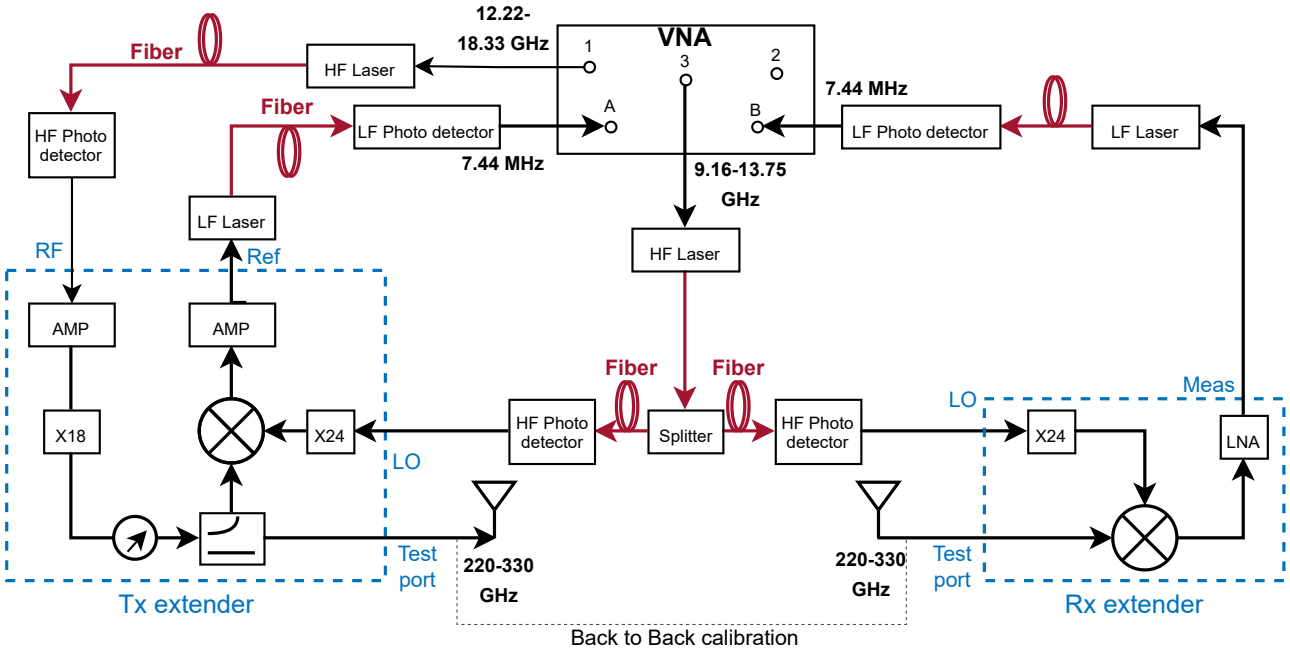

Fig. 3. Block diagram of the 300 GHz system

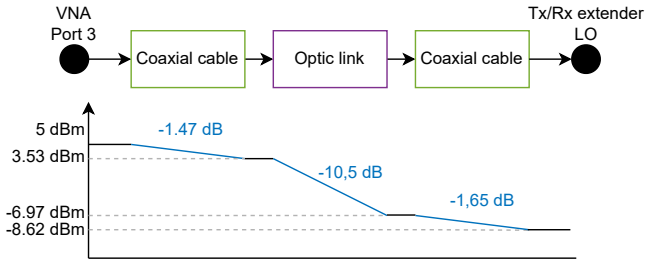

Fig. 4. Link budget for LO chain. The link budget is performed at a test frequency of 300 GHz corresponding to LO frequency at 12.5 GHz

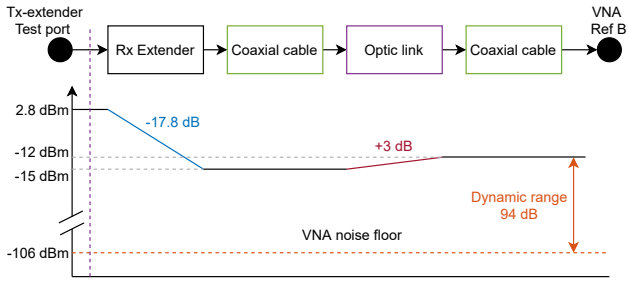

Fig. 5. Link budget for the link between port 1 and Tx extender RF port. The link budget is performed at 300 GHz

the total losses from coaxial cable is 3.1 dB giving a power of -8.6 dBm at the LO port at the frequency extenders.

The reference signal chain from the testport to the VNA reference port B is shown, as the power at port A is constant and not dependent on the channel. The output power is 2.8 dBm at the Tx testport, and there is a loss of -17.8 dB at the Rx extender. The Optic link gives a gain of +3 dB giving a power at the ref port B at -12 dBm, a graph of the gains can be seen in Fig. 5. The achieved dynamic range of the channel sounder at 300 GHz is 94 dB in the back-to-back measurement. Note that similar to the 28 GHz system, a larger dynamic range can be achieved if we lower the system IF bandwidth, which will also increase the measurement time.

Note that for our work in this paper, we measured the channel spatial profile based on the direct scanning scheme. That is, we can directly measure the channel spatial profile based on channel impulse response measurements for each rotation, and therefore the phase measurements among different rotations are not important. The phase stability is therefore not discussed in the paper. However, for phase critical channel sounding applications, e.g. virtual array solution, phase stability is of high importance and should be properly addressed, as discussed in [13], [22].

III. Measurement Setup

Two measurements based on the developed channel sounders are presented, one with a distance of 43 m between Tx and Rx, and the other one with a distance of 27 m. Both measurements took place at the same location shown in Fig. 9. The turntables at the Rx and Tx side are shown in Fig. 10. Long-range capabilities of the 300 GHz system are demonstrated with a point-to-point measurement at 43 m, i.e. with Tx and Rx antenna pointing to each other. The 27 m measurement uses rotation tables to obtain directional information for the MPC. Furthermore, comparisons between 28 GHz and 300 GHz are made based on the 27 m measurement. The directional scanning scheme (DSS), i.e. via rotating directive antenna to obtain the channel spatial profile with the help of

turntable, is the most popular scheme due to its simplicity and good system dynamic range offered by the directive antennas.

For 300 GHz system, horn antennas with a Half Power Beamwidth (HPBW) of 8° and a gain at 25 dBi are used both at the Tx and Rx side. When performing the 47 m measurement the antennas are pointing at each other (i.e. point-to-point measurement). For the 23 m measurement a turntable rotating the Rx antenna 360 degrees in the azimuth was used to measure MPC arriving at different angles. For the Tx antenna a turntable rotating 180° in the azimuth plane was employed, to imitate an omnidirectional antenna. The Tx turntable is rotated in steps of 4° yielding a total of $N_\phi = 46$ Tx turntable steps. For each Tx angle a full rotation in steps of 4 degrees of the Rx table is made, giving a full round $N_\theta = 90$ steps, the total sum of measurement points is 4140 when combining the Rx rotation and Tx rotation.

For the 28 GHz system a 360° turntable stepping in 4° was used for rotating the Rx antenna. An omni-directional antenna was used for the Tx antenna. Therefore no rotation was done with the Tx antenna. The 28 GHz measurement was performed by measuring at each 4° degree step at the Rx antenna, yielding $N_\theta = 90$ steps.

The Tx and Rx antennas were placed at a height of 1.20 meters in both the 27 and 43 m measurements. A layout of the measurement environment can be seen in Fig. 14. The 43 m measurement was performed with the Tx and Rx being placed at each end of the corridor obtaining the furthest possible distance in the given environment. Tx was placed at one end of the corridor, and Rx in the middle of the open area for the 27 m measurements as shown in Fig. 14.

With the turntable system only 2D azimuth resolution is measured. The antennas HPBW in the elevation is 19 degrees and 16.5 degrees for the 28 GHz horn antenna and bi-conical antenna respectively. For the 300 GHz the HPBW of the horn antenna in the elevation is 6 degree, the radiation pattern can be seen in Fig. 6. The possible paths in the elevation plane is from reflections of the ceiling and ground. The elevation of arrival is 5.0 degrees and 6.8 degrees for ground reflection and ceiling reflection respectively. Comparing the radiation pattern for the two systems shown in Fig. 6 and the elevation-of-arrival, a gain difference of 5 dB is seen for the ground reflection and a gain difference of 6.4 dB is seen for the ceiling reflection between the 28 GHz and 300 GHz system.

The settings for the 300 GHz and 28 GHz systems can be seen in Table II and are similar for both the 43 m and 27 m measurements. The measurements were performed with a bandwidth of 2 GHz giving a delay resolution $\Delta\tau$ of 0.5 ns according to,

$$\Delta\tau = \frac{1}{BW} \tag{3}$$

Therefore MPCs more than 15 cm apart can be detected in principle in the delay domain. The number of frequency points N_f was set to 1001, giving a frequency step of 2 MHz. Therefore, a maximum excess delay of 90 ns corresponding to a max distance of 150 m can be achieved, according to.

$$\tau_{max} = \frac{1}{\Delta f} \tag{4}$$

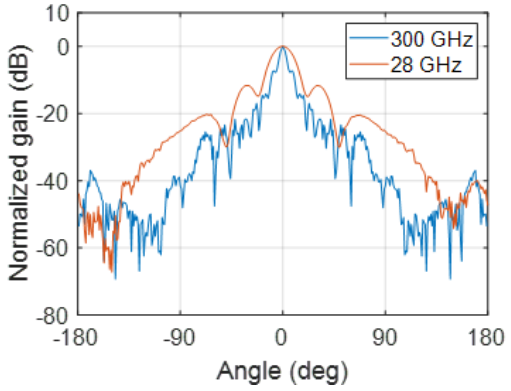

Fig. 6. Elevation radiation pattern

TABLE II
MEASUREMENTS CONFIGURATION FOR THE 300 GHZ AND 28 GHZ SYSTEM

Parameter	300 GHz	28 GHz
Start frequency f_s (GHz)	299	28
End frequency f_e (GHz)	301	30
Bandwidth (BW) (GHz)	2	2
Frequency points N_f	1001	1001
Maximum excess delay τ_{max}	90 ns	90 ns
Maximum detecting distance d_{max}	150	150
Time domain resolution $\Delta\tau$	500 ps	500 ps
Spatial resolution	15 cm	15 cm
Tx Antenna HPBW	8°	Bi-conical
Tx Antenna gain	25 dB	5 dB
Rx Antenna HPBW	8°	8°
Rx Antenna gain	25 dB	20 dB
Number of Tx steps	46	-
Tx step angle	4°	4°
Number of Rx steps	90	90
Rx step angle	4°	4°

Back to back calibration was performed both for the 28 GHz and 300 GHz system before the measurement campaign, and the results for the 300 GHz were reported here. In Fig. 7 the system frequency responses before and after calibration are shown, the time delay responses can be seen in Fig. 8. A flat frequency response is achieved after calibration and only the direct cable path is seen in the time domain after calibration as expected. Before the calibration, the system frequency response is not flat, as expected.

IV. RESULTS

Results from measurements at 47 m and 23 m are presented in Section IV-A and Section IV-B respectively.

A. *Point-to-point measurement at 43 m*

Since no directional data was measured for the 43 m measurement, the Channel Impulse Response (CIR) was directly obtained by doing an Inverse Discrete Fourier Transform (IDFT) over the measured data. The CIR can then be written as a sum of the MPC for each time delay τ.

$$h(\tau) = \sum_{l=1}^{L} \alpha_l \delta(\tau - \tau_l) \tag{5}$$

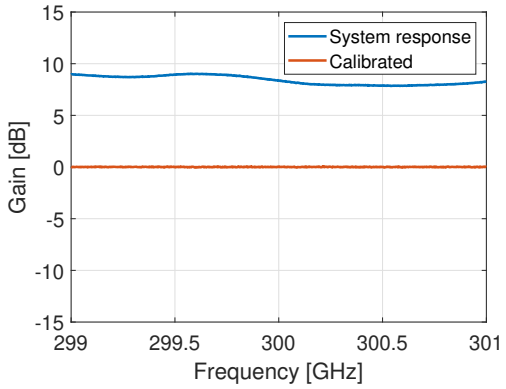

Fig. 7. Back to back frequency response and calibration of the 300 GHz system

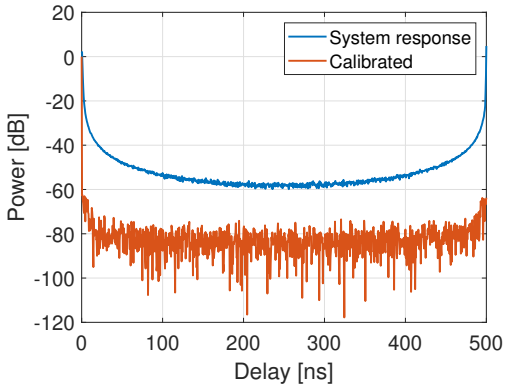

Fig. 8. Back to back delay domain response for the 300 GHz system before and after calibration

Fig. 9. Picture of the measurement environment

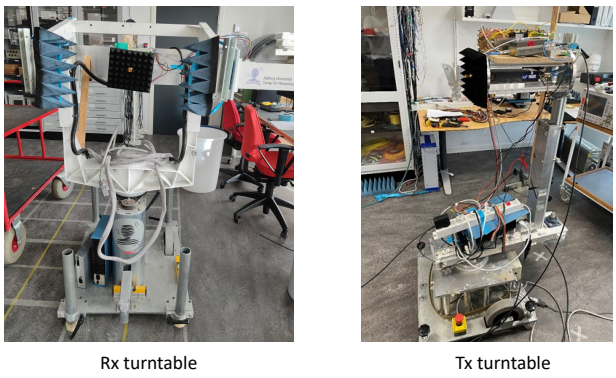

Fig. 10. Picture of turntables at the Rx and Tx side.

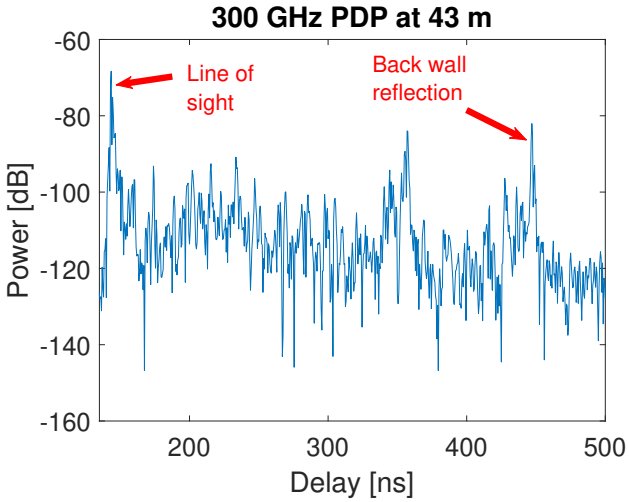

Fig. 11. PDP for a measurement with a distance of 43 m between Tx and Rx. A Hanning windows was applied doing the IDFT

In Fig. 11 the measured CIR can be seen. The highlighted "Line of sight" area on Fig. 11 corresponds to MPCs arriving directly to the Rx. The component arriving at 143.5 ns, corresponds to a distance of 43 m which corresponds to the distance between the Tx and Rx. The highlighted "Back wall reflection" in Fig. 11 is the group of MPCs which are reflected on the back of the corridor. The peak at 447 ns corresponds to a distance of 134 m, corresponding to the distance from Tx to the wall behind the Rx reflecting back to the wall behind the Tx and back arriving at the Rx. The noise floor for the measurements is approximately around -100 dB. The LOS and MPC are at -69 dB and -82 dB giving a dynamic range of 30 dB. The system is therefore capable of making measurements at a distance of 43 m.

B. Double directional measurement at 23m

When using directional antennas for both the Tx and Rx on a rotational table, the CIR can be characterized by the delay τ, the Angle of Arrival (AOA) θ, and Angle of Departure (AOD) ϕ. The CIR is therefore written as,

$$h(\tau,\theta,\phi) = \sum_{l=1}^{L} \alpha_l \delta(\tau-\tau_l)\delta(\phi-\phi_l)\delta(\theta-\theta_l) \qquad (6)$$

An approximation of an omnidirectional transmitting antenna from the transmitter horn antenna for the 300 GHz system was made to compare it with the results from the 28 GHz system. The approximation was obtained by the maximum the power for each θ Rx rotations over all ϕ Tx rotation [40],

$$PADP(\tau,\theta) = \max_{\phi} |h(\tau,\phi,\theta)|^2 \tag{7}$$

A Power Angle Delay Profile (PADP) is therefore calculated for both the 28 GHz system and the 300 GHz system, and a plot can be seen in Fig. 12. Areas in the PADP in Fig. 12 have been highlighted for comparison with the PDP in Fig. 13 and Fig. 14. In Table III the highlighted main paths is shown in details. The dynamic range of the plot in Fig. 12 is set to 30 dB, and therefore not all the MPC showing up at the PADP plot can be seen. Four main MPCs are observed at the plots. The MPC are stronger for the 28 GHz measurement compared to the observation for the 300 GHz which is expected.

A PDP was calculated by maximazing over all angles for each delay [40].

$$PDP(\tau) = \max_{\phi}\max_{\theta} |h(\tau,\phi,\theta)|^2 \tag{8}$$

A plot of the PDP for the 300 GHz and 28 GHz system can be seen in Fig. 13. In Fig. 12 main paths areas are highlighted for comparison with the PADP in Fig. 13.

Furthermore, a PAS was calculated by summing the delay for each Tx and Rx angle for the 300 GHz measurement [40].

$$PAS(\phi,\theta) = \sum_{N_\tau} |h(\tau,\phi,\theta)|^2 \tag{9}$$

A plot of the PAS for 300 GHz can be seen in Fig. 15, since the delay are added the noise floor will be added up too. The MPC AOA are centered around 90° and 270°, which can be seen even when the AOD is varied between 0° and 180°. The power mainly comes from the LOS and reflections of the wall behind Tx and Rx.

Estimated trajectory of the MPC are drawn in Fig. 14 with respective numbering. Comparing Fig. 13 with Fig. 12 it can be seen that the MPCs with highest power correspond to either a LOS component arriving directly or components hitting the back wall of the corridor. The delay times of the power maxima at the areas highlighted in Fig. 13 and Fig. 12 labeled 1, 2, 3 correspond to distance of 27 m, 62 m and 125 m respectively. 27 m is the direct distance between Tx and Rx, 62 m is the distance from the Tx to the back wall then reflected back to the Rx and 125 m from Tx hitting both the wall behind Tx and Rx, then arriving at the receiver. Within the labeled area 1 on Fig. 13, a MPC for the 28 GHz system can be observed at 94.5 ns corresponding to 28.3 m, and it is expected to be from reflection of the walls in the corridor. This MPC is however, not seen at 300 GHz.

Observing the PAS plotted in Fig. 15 the main energy is also located at a receiving angle of 90° and 270°. In [11] measurements with Tx and Rx placed closer than this measurement were performed, only LOS and reflection from the back wall were observed. The measurements are also similar to the results of [22] where a total of 4 MPCs were

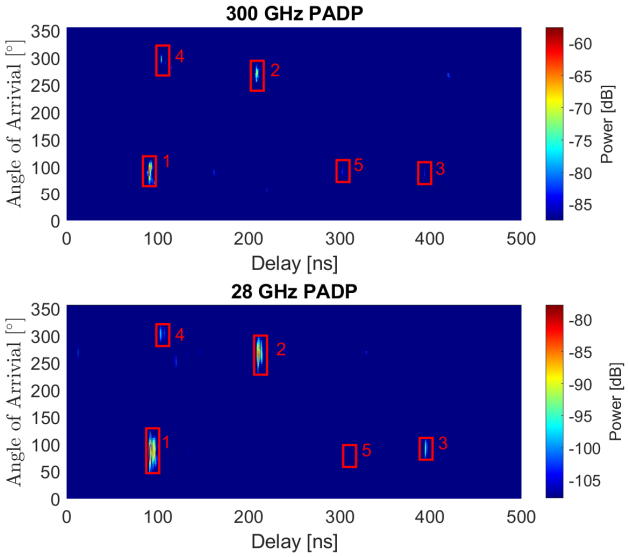

Fig. 12. PADP for the 300 and 28 GHz system a Hanning window was applied doing the IDFT to reduce the side lobes.

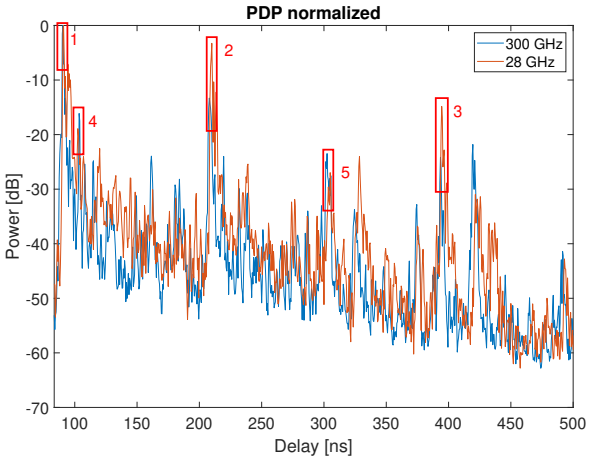

Fig. 13. PDP for the 300 and 28 GHz system a Hanning window was applied doing the IFFT to reduce the side lobes

observed mainly from the LOS component or reflections from back walls.

The MPCs labeled 4 and 5 in Fig. 13 are observed to come from a different angle than 90° or 270° and are observed for both the 300 GHz and 28 GHz measurements. It is suspected to come from reflections of the area below the Rx antenna on Fig. 14.

Comparing the PDP and PADP for 28 GHz and 300 GHz the same main MPCs can be seen. At label 4 and 5 a higher power is observed for the 300 GHz measurement compared to the 28 GHz system which is not expected. Though the system was carefully calibrated and positioned, small misalignment in the placement can have happened. The antenna used for the 300 GHz systems was two highly directive antennas with a total of 50 dBi antenna gain, at 28 GHz a horn antenna and an omnidirectional antenna was used having a total of 30 dBi antenna gain. The antenna gain is different for

TABLE III
THE POWER, DELAY, AND ANGLE INFORMATION OF THE MAIN PATHS IN THE MEASUREMENTS.

Path index	300 GHz Power [dB]	300 GHz Delay [ns]	300 GHz AoA [°]	300 GHz AoD [°]	28 GHz Power [dB]	28 GHz Delay [ns]	28 GHz AoA [°]
1	-57.6	90.5	88	88	-77.8	91	80
2	-70.9	208	268	92	-91.1	210	264
3	-81.8	393.5	84	88	-92.7	394.5	88
4	-73.7	103.5	296	96	-98.7	102.5	300
5	-81	302.5	92	88	-104.8	305	84

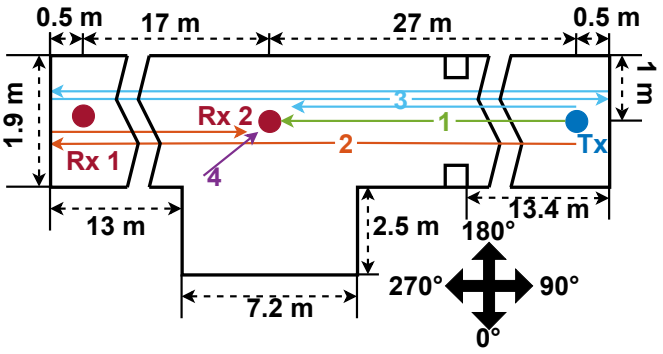

Fig. 14. Illustration of the measurement area. The Rx 1 placement is for the 43 meter measurement and Rx 2 is for the 23 meter measurement. The drawn MPC are for the 23 meter measurement.

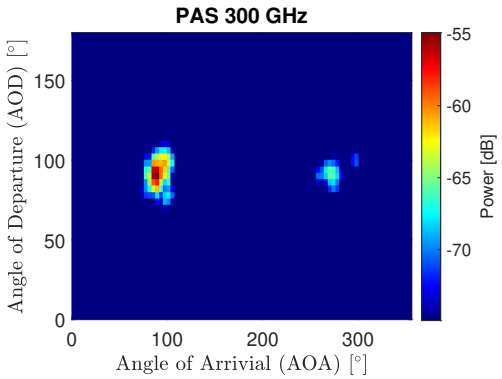

Fig. 15. PAS for 300 GHz

the two systems may cause power differences of the paths. Furthermore, the measurement systems fixtures are different for the two systems, the 300 GHz system have a frequency extender behind each antenna, in the 30 GHz system only antennas are at the measurement position.

From Fig. 13 it is seen that the MPCs are more spread and many arriving at later delay compared with the 300 GHz system. The average delay μ_{DS} and root mean squared (rms) delay spread σ_{DS} of the PDP for in Fig. 13 have been calculated using Equation (10) and Equation (11) respectively.

$$\mu_{DS} = \frac{\sum_{\tau} \tau PDP(\tau)}{\sum_{\tau} PDP(\tau)} \tag{10}$$

$$\sigma_{DS} = \sqrt{\frac{\sum_{\tau} (\tau - \mu_{DS})^2 PDP(\tau)}{\sum_{\tau} PDP(\tau)}} \tag{11}$$

For the full dynamic range of the PDP, Fig. 13, the average delay and the rms delay spread have been calculated to 134 ns, 66 ns for 28 GHz, and 107 ns, 51 ns for 300 GHz, respectively. Using the PDP with dynamic range at 30 dB the average delay and rms delay spread was calculated to 132 ns, 64 ns for 28 GHz and 104 ns, 46 ns for 300 GHz, respectively. The difference between full dynamic range and 30 dB is therefore limited, and mainly caused by the many weak MPCs ignored in the 30dB dynamic range. Millimeter wave and sub-THz communication will rely on dominant propagation paths. This is also supported by the observation that minor differences can be observed by different dynamic range settings. From the observed main paths shown in Table III the AoA angular spreads at the two frequency bands was calculated as the second central-moment of the azimuth-power spectrum in Equation (12)

$$\sigma_{\theta} = \sqrt{\frac{\sum_{\theta} (\theta - \mu_{\theta})^2 P(\theta)}{\sum_{\theta} P(\theta)}} \tag{12}$$

Where the mean azimuth μ_{θ} is calculated as,

$$\mu_{\theta} = \frac{\sum_{\theta} P(\theta)}{\sum_{\theta} P(\theta)} \tag{13}$$

The calculated angular spreads are 98.3 and 95.5 degrees for 28 GHz and 300 GHz.

The ratio between the power of the main LOS component and the MPCs were calculated to be 0.85 and 0.68 for the 300 GHz and 28 GHz system respectively. From the normalized PDP in Fig. 13, the differences between the MPCs for the 300 and 28 GHz system are 2.8 dB, -10.0 dB, 3.5 dB and -9.3 dB for the numbered areas 2 to 5, respectively. The back reflection losses, represented by MPCs 2 and 3, are therefore much higher at 300 GHz compared to 28 GHz. MPCs 4 and 5 have a lower power loss at 300 GHz, but the difference is not as significant.

V. CONCLUSION

VNA based channel sounders for long range channel sounding at 300 GHz and 28 GHz were described. Link budget analysis for both channel sounder systems were made. A measurement campaign in a corridor with both setups was performed. The environment and placement of both systems were identical for the measurements, making it possible to compare the MPCs at the two frequencies. Only LOS and

MPCs from reflection of the back wall were observed for the 300 GHz system. However, the 28 GHz system showed further MPCs from reflection of the side walls. The propagation loss for 300 GHz is therefore concluded to be higher than for the 28 GHz. Models that can predict 28 GHz propagation do therefore not necessarily perfectly scale to 300 GHz, yet main MPCs seem to be similar. The LOS component is observed to be dominant compared to other MPCs for both the 300 GHz and 28 GHz in the LOS scenario as expected.

Further work should be done, where other channel scenarios (especially outdoor) are measured. Longer distance measurements than the presented should be performed to further investigate the propagation properties at 300 GHz. The proposed system is capable of measuring at a larger distance than presented in this paper. Furthermore, other channel scenarios should be investigated, since only measurements were performed in a corridor environment and the results might be different in more open areas. With a larger amount of measurement campaigns performed both at long range and short range and different channel scenarios, sub-THz channel models should be investigated and developed.

Acknowledgment

A thanks to Kim Olesen, Zhiqiang Yuan and Huaqiang Gao for helping with the measurements.

References

[1] T. S. Rappaport, S. Sun, R. Mayzus, *et al.*, "Millimeter wave mobile communications for 5G cellular: It will work!" *IEEE Access*, vol. 1, pp. 335–349, 2013. DOI: 10.1109/ACCESS.2013.2260813.

[2] T. S. Rappaport, Y. Xing, O. Kanhere, *et al.*, "Wireless communications and applications above 100 GHz: Opportunities and challenges for 6G and beyond," *IEEE Access*, vol. 7, pp. 78 729–78 757, 2019. DOI: 10.1109/ACCESS.2019.2921522.

[3] *IEEE Std 802.15.3d-2017 (Amendment to IEEE Std 802.15.3-2016 as amended by IEEE Std 802.15.3e-2017)*,

[4] FCC, *Fcc opens spectrum horizons for new services and technologie*. [Online]. Available: https://www.fcc.gov/document/fcc-opens-spectrum-horizons-new-services-technologies.

[5] T. Schneider, A. Wiatrek, S. Preussler, M. Grigat, and R.-P. Braun, "Link budget analysis for terahertz fixed wireless links," *IEEE Transactions on Terahertz Science and Technology*, vol. 2, no. 2, pp. 250–256, 2012. DOI: 10.1109/TTHZ.2011.2182118.

[6] Y. Xing and T. S. Rappaport, "Propagation Measurement System and Approach at 140 GHz-Moving to 6G and Above 100 GHz," in *2018 IEEE Global Communications Conference (GLOBECOM)*, 2018, pp. 1–6. DOI: 10.1109/GLOCOM.2018.8647921.

[7] K. Rikkinen, P. Kyosti, M. E. Leinonen, M. Berg, and A. Parssinen, "THz radio communication: Link budget analysis toward 6G," *IEEE Communications Magazine*, vol. 58, no. 11, pp. 22–27, 2020. DOI: 10.1109/MCOM.001.2000310.

[8] A. F. Molisch, *Wireless Communications*. John Wiley & Sons, 2005, ISBN: 978-0-470-84888-3.

[9] K. HANEDA, "Channel models and beamforming at millimeter-wave frequency bands," *IEICE TRANS. COMMUN*, vol. E98-B, no. 5, pp. 755–767, 2015. DOI: 10.1109/TCOMM.2020.3001614.

[10] Y. Lyu, P. Kyösti, and W. Fan, "Sub-Terahertz Channel Sounder: Review and Future Challenges," *China Communications*, Oct. 2021.

[11] ——, "Sub-THz VNA-based channel sounder structure and channel measurements at 100 and 300 GHz," in *2021 IEEE 32nd Annual International Symposium on Personal, Indoor and Mobile Radio Communications (PIMRC)*, 2021, pp. 1–5. DOI: 10.1109/PIMRC50174.2021.9569702.

[12] P. Kyösti, K. Haneda, J.-M. Conrat, and A. Pärssinen, "Above-100 GHz wave propagation studies in the european project Hexa-X for 6G channel modelling," in *2021 Joint European Conference on Networks and Communications & 6G Summit (EuCNC/6G Summit)*, IEEE, 2021, pp. 538–543.

[13] A. Mbugua, W. Fan, X. Cai, *et al.*, "System Development and Experimental Validation of a Long Range VNA-Based Channel Sounder," *IEE Proceedings - Microwaves Antennas and Propagation*, vol. 14, May 2020. DOI: 10.1049/iet-map.2019.0923.

[14] Y. Lyu, P. Kyösti, and W. Fan, "Sub-THz VNA-based Channel Sounder Structure and Channel Measurements at 100 and 300 GHz," in *2021 IEEE 32nd Annual International Symposium on Personal, Indoor and Mobile Radio Communications (PIMRC)*, IEEE, 2021, pp. 1–5.

[15] Y. Lyu, A. W. Mbugua, K. Olesen, P. Kyösti, and W. Fan, "Design and validation of the phase-compensated long-range sub-THz VNA-based channel sounder," *IEEE Antennas and Wireless Propagation Letters*, vol. 20, no. 12, pp. 2461–2465, 2021.

[16] L. Pometcu and R. D'Errico, "An Indoor Channel Model for High Data-Rate Communications in D-Band," *IEEE Access*, vol. 8, pp. 9420–9433, 2020. DOI: 10.1109/ACCESS.2019.2960614.

[17] Z. Yu, Y. Chen, G. Wang, W. Gao, and C. Han, "Wideband Channel Measurements and Temporal-Spatial Analysis for Terahertz Indoor Communications," in *2020 IEEE International Conference on Communications Workshops (ICC Workshops)*, 2020, pp. 1–6. DOI: 10.1109/ICCWorkshops49005.2020.9145314.

[18] N. A. Abbasi, A. Hariharan, A. M. Nair, *et al.*, "Double Directional Channel Measurements for THz Communications in an Urban Environment," in *ICC 2020 - 2020 IEEE International Conference on Communications (ICC)*, 2020, pp. 1–6. DOI: 10.1109/ICC40277.2020.9148631.

[19] S. L. H. Nguyen, J. Jarvelainen, A. Karttunen, K. Haneda, and J. Putkonen, "Comparing Radio Propagation Channels Between 28 and 140 GHz Bands in a Shopping Mall," *ArXiv*, vol. abs/1712.09438, 2017.

[20] S. L. H. Nguyen, K. Haneda, J. Järveläinen, A. Karttunen, and J. Putkonen, "Large-scale parameters of

spatio-temporal short-range indoor backhaul channels at 140 GHz," in *2021 IEEE 93rd Vehicular Technology Conference (VTC2021-Spring)*, 2021, pp. 1–6. DOI: 10.1109/VTC2021-Spring51267.2021.9448958.

[21] S. Sun, T. A. Thomas, T. S. Rappaport, H. Nguyen, I. Z. Kovacs, and I. Rodriguez, "Path Loss, Shadow Fading, and Line-of-Sight Probability Models for 5G Urban Macro-Cellular Scenarios," in *2015 IEEE Globecom Workshops (GC Wkshps)*, 2015, pp. 1–7. DOI: 10.1109/GLOCOMW.2015.7414036.

[22] A. W. Mbugua, W. Fan, K. Olesen, X. Cai, and G. F. Pedersen, "Phase-compensated optical fiber-based ultrawideband channel sounder," *IEEE Transactions on Microwave Theory and Techniques*, vol. 68, no. 2, pp. 636–647, 2020. DOI: 10.1109/TMTT.2019.2948842.

[23] K. Haneda, L. Tian, H. Asplund, *et al.*, "Indoor 5G 3GPP-like channel models for office and shopping mall environments," in *2016 IEEE International Conference on Communications Workshops (ICC)*, 2016, pp. 694–699. DOI: 10.1109/ICCW.2016.7503868.

[24] J. Vehmas, J. Jarvelainen, S. L. H. Nguyen, R. Naderpour, and K. Haneda, "Millimeter-Wave Channel Characterization at Helsinki Airport in the 15, 28, and 60 GHz Bands," in *2016 IEEE 84th Vehicular Technology Conference (VTC-Fall)*, 2016, pp. 1–5. DOI: 10.1109/VTCFall.2016.7881086.

[25] M. Sasaki, W. Yamada, T. Sugiyama, M. Mizoguchi, and T. Imai, "Path loss characteristics at 800 MHz to 37 GHz in urban street microcell environment," in *2015 9th European Conference on Antennas and Propagation (EuCAP)*, 2015, pp. 1–4.

[26] R. J. Weiler, M. Peter, T. Kühne, M. Wisotzki, and W. Keusgen, "Simultaneous millimeter-wave multi-band channel sounding in an urban access scenario," in *2015 9th European Conference on Antennas and Propagation (EuCAP)*, 2015, pp. 1–5.

[27] R. Naderpour, J. Vehmas, S. Nguyen, J. Järveläinen, and K. Haneda, "Spatio-temporal channel sounding in a street canyon at 15, 28 and 60 GHz," in *2016 IEEE 27th Annual International Symposium on Personal, Indoor, and Mobile Radio Communications (PIMRC)*, 2016, pp. 1–6. DOI: 10.1109/PIMRC.2016.7794730.

[28] S. Priebe, C. Jastrow, M. Jacob, T. Kleine-Ostmann, T. Schrader, and T. Kürner, "channel and propagation measurements at 300 GHz," *IEEE Transactions on Antennas and Propagation*,

[29] Y. Zantah, F. Sheikh, A. A. Abbas, M. Alissa, and T. Kaiser, "Channel measurements in lecture room environment at 300 GHz," in *2019 Second International Workshop on Mobile Terahertz Systems (IWMTS)*, 2019, pp. 1–5. DOI: 10.1109/IWMTS.2019.8823666.

[30] K. Guan, B. Ai, D. He, *et al.*, "Channel sounding and ray tracing for THz channel characterization," in *2020 13th UK-Europe-China Workshop on Millimetre-Waves and Terahertz Technologies (UCMMT)*, 2020, pp. 1–3. DOI: 10.1109/UCMMT49983.2020.9295992.

[31] E. M. Vitucci, M. Zoli, F. Fuschini, *et al.*, "Tri-band mm-wave directional channel measurements in indoor environment," in *2018 IEEE 29th Annual International Symposium on Personal, Indoor and Mobile Radio Communications (PIMRC)*, 2018, pp. 205–209. DOI: 10.1109/PIMRC.2018.8580770.

[32] K. Guan, B. Peng, D. He, *et al.*, "Channel Sounding and Ray Tracing for Train-to-Train Communications at the THz Band," in *2019 13th European Conference on Antennas and Propagation (EuCAP)*, 2019, pp. 1–5.

[33] J. M. Eckhardt, V. Petrov, D. Moltchanov, Y. Koucheryavy, and T. Kürner, "Channel measurements and modeling for low-terahertz band vehicular communications," *IEEE Journal on Selected Areas in Communications*, vol. 39, no. 6, pp. 1590–1603, 2021. DOI: 10.1109/JSAC.2021.3071843.

[34] C. Jansen, S. Priebe, C. Moller, *et al.*, "Diffuse Scattering From Rough Surfaces in THz Communication Channels," *IEEE Transactions on Terahertz Science and Technology*, vol. 1, no. 2, pp. 462–472, 2011. DOI: 10.1109/TTHZ.2011.2153610.

[35] R. Piesiewicz, C. Jansen, D. Mittleman, T. Kleine-Ostmann, M. Koch, and T. Kurner, "Scattering Analysis for the Modeling of THz Communication Systems," *IEEE Transactions on Antennas and Propagation*, vol. 55, no. 11, pp. 3002–3009, 2007. DOI: 10.1109/TAP.2007.908559.

[36] S. Rey, J. M. Eckhardt, B. Peng, K. Guan, and T. Kürner, "Channel sounding techniques for applications in THz communications: A first correlation based channel sounder for ultra-wideband dynamic channel measurements at 300 GHz," in *2017 9th International Congress on Ultra Modern Telecommunications and Control Systems and Workshops (ICUMT)*, 2017, pp. 449–453. DOI: 10.1109/ICUMT.2017.8255203.

[37] M. Mechaik, "Signal attenuation in transmission lines," in *Proceedings of the IEEE 2001. 2nd International Symposium on Quality Electronic Design*, 2001, pp. 191–196. DOI: 10.1109/ISQED.2001.915226.

[38] C.-L. Cheng, S. Sangodoyin, and A. Zajić, "THz Cluster-Based Modeling and Propagation Characterization in a Data Center Environment," *IEEE Access*, vol. 8, pp. 56 544–56 558, 2020. DOI: 10.1109/ACCESS.2020.2981293.

[39] VDI Virginia Diodes Inc, *VNA extension modules operational manual*, 2021. [Online]. Available: https://vadiodes.com/images/Products/VNA/Product_Manual/VDI-707.1-VNAx-Product-Manual.pdf.

[40] C. U. Bas, R. Wang, S. Sangodoyin, *et al.*, "28 GHz Microcell Measurement Campaign for Residential Environment," in *GLOBECOM 2017 - 2017 IEEE Global Communications Conference*, 2017, pp. 1–6. DOI: 10.1109/GLOCOM.2017.8254897.